Journal of
Marine Science and Engineering

MDPI

Article

Modeling the Impact of the Implementation of a Submerged Structure on Surf Zone Sandbar Dynamics

Clément Bouvier [1,2,*], Bruno Castelle [2] and Yann Balouin [1]

[1] BRGM, Occitanie-Pyrénées-Méditerranée (SGR/LRO), 1039 Rue de Pinville, 34000 Montpellier, France; y.balouin@brgm.fr
[2] CNRS, UMR EPOC, University Bordeaux, Allée Geoffroy Saint-Hilaire, CS 50023, 33615 Pessac, France; clement.bouvier@u-bordeaux.fr (C.B.); bruno.castelle@u-bordeaux.fr (B.C.)
* Correspondence: c.bouvier@brgm.fr

Received: 4 April 2019; Accepted: 19 April 2019; Published: 25 April 2019

Abstract: Coastal defense strategies based on structures are increasingly unpopular as they are costly, leave lasting scars on the landscape, and sometimes have limited effectiveness or even adverse impacts. While a clear improvement concerning aesthetic considerations using soft submerged breakwater is undeniable, their design has often focused on wave transmission processes across the crest of the structure, overlooking short- to medium-term morphodynamic responses. In this study, we used a time- and depth-averaged morphodynamic model to investigate the impact of the implementation of a submerged breakwater on surf zone sandbar dynamics at the beach of Sète, SE France. The hydrodynamic module was calibrated with data collected during a field experiment using three current profilers deployed to capture rip-cell circulation at the edge of the structure. The model showed good agreement with measurements, particularly for the longshore component of the flow (RMSE = 0.07 m/s). Results showed that alongshore differential wave breaking at the edge of the submerged breakwater drove an intense (0.4 m/s) two-dimensional circulation for low- to moderate-energy waves. Simulations indicated that inner-bar rip channel development, which was observed prior to the submerged reef implementation, was inhibited in the lee of the structure as rip-cell circulation across the inner bar disappeared owing to persistently low-energy breaking waves. The cross-shore sandbar dynamics in the lee of the structure were also impacted due to the drastic decrease of the offshore-directed flow over the inner-bar during energetic events. This paper highlights that implementation of a submerged breakwater results in larges changes in nearshore hydrodynamics that, in turn, can affect overall surf zone sandbar behavior.

Keywords: submerged breakwater; morphodynamic model; sandbar dynamics

1. Introduction

Coastal protection hard structures such as groynes, breakwaters, seawalls, and revetments have been implemented worldwide to limit coastal erosion and to provide flooding protection to the hinterland [1,2]. However, this traditional coastal defense strategy is increasingly unpopular, as it is costly, leaves lasting scars on the landscape, and sometimes has limited effectiveness or even adverse impacts [3,4]. Mimicking natural reefs, the idea to implement submerged breakwaters (SBWs) a few hundred meters from the shore appeared rapidly [5,6]. While clear aesthetic improvement using such structures compared with classical coastal management practices is not questionable, SBWs have been often designed only considering wave transmission processes across the crest of the structure [7]. The design of SBWs not only depends on certain short timescale considerations, such as wave energy [8],

wave breaking [9], wave set-up [10], or scour characteristics [11], the short- to medium-term (storms to decade) morphodynamic responses and shoreline evolution resulting from SBW deployment need to be carefully considered as well.

The recent amount of defecting SBW deployments driving increased shoreline erosion [12] confirms the importance of understanding the complex influence of the structure on the mode of shoreline response. Field observations reveal that formation of a salient or any shoreline accretion pattern is not dictated by wave energy dissipation considerations in the lee of the SBWs [13–15]. To help coastal engineers to design efficient SBWs, a better understanding of the interplay between the structure characteristics, wave transformation, and wave-driven currents is required.

Traditionally, the study of the effects of SBWs in terms of transmission, reflection, and wave overtopping has been done in flume experiments, in which only one horizontal direction is considered. However, a proper understanding of the effects of SBWs on nearshore waves and horizontal circulation is necessary for the calculation of sediment transport and morphological evolution [16,17]. These structures result in wave energy dissipation through depth-induced wave breaking. At the alongshore edges of the SBW, adjacent regions of breaking and non-breaking waves form a large differential in wave forcing and, in turn, a vertical vorticity forcing [18], which is key to rip-flow circulation formation [19]. This results in two-dimensional horizontal (2DH) flow and sediment transport patterns [17].

The published literature primarily reports the use of two types of numerical models to simulate shoreline response to SBWs, namely one-line models and 2DH (depth-averaged) coastal area models. Applicability of one-line models, which all predict the formation of salient or tombolo in the lee of the structure when breaking occurs, is questionable as the role of 2DH nearshore circulation is disregarded. Contrarily, 2DH models are capable of reproducing two-dimensional complex nearshore circulation making them more suitable to study shoreline response to SBWs. However, when sediment transport and morphological changes are switched on, the strongly nonlinear nature of these models can result in an inescapable build-up of errors and unreliable simulations on long timescales. For instance, simulating the morphological behavior of the shoreface at a highly protected beach (Punta Marina, Italy) was challenging [20], primarily because of the long time series addressed, the difficulty to correctly account for permeable reef structure, and inaccurate cross-shore sediment transport parametrization. Therefore, morphological changes are often switched off to address the influence of the SBW in terms of hydrodynamics only.

Using 2DH numerical models or 2D laboratory experiments, several relationships elucidated the influence of SBW characteristics on hydrodynamics and shoreline response. The first empirical relationship was obtained from observations on natural reefs [5] linking shoreline response (salient formation) and natural reef characteristics (length and width). The equation was then revised considering surf zone width, SBW position (distance from the shore) and wave incidence [17]. More recently, shoreline response appeared to be driven by additional SBW characteristics (depth from the crest to the surface, width, or position) and wave conditions (wave height and direction) using nearshore circulation patterns as an indication of the mode of shoreline response [21]. Nevertheless, results indicated that shoreline response to SBW implementation was governed by 2DH nearshore circulation patterns, consisting of longshore flows in the lee of the structures, and offshore flow outside. Shoreline accretion/erosion patterns depend on the cross-shore position of those circulations. Noteworthy, to our knowledge, most of the numerical experiments were undertaken on idealized [17,21] and real [22] cases consisting of alongshore uniform, non-barred beach morphology and overlooking potential feedback with nearshore sandbar(s).

Nearshore sandbars potentially enforce alongshore morphological variability at the beach up to the shoreline and the coastal dune (e.g., [23–25]). Recent developments of video monitoring techniques can provide high-frequency, remotely sensed optical information from which morphological changes and hydrodynamic data can be derived. Shoreline–sandbar geometry as well as rip-channel positions have long been measured with reasonable accuracy using video stations (e.g., [26–31]). Based on such

techniques, recent observations at the Lido of Sète (SE France) evidenced the impact of an SBW 800 m in length and 12 m in width on the nearshore system, particularly on the response of the coupled shoreline–sandbar system [32]. The authors showed that the expected salient formation was not observed. Instead, shoreline coupled to the modified sandbar geometry, which resulted in a slight seaward migration of the shoreline in front of the structure. Overall, this study highlighted that the role of the sandbar was critical to shoreline response to the implementation of SBWs on barred beaches [32,33].

This paper aims to characterize for the first time the complex 2DH nearshore circulation induced by SBWs at the Lido of Sète by combining field observations and numerical modeling. After a comparison between measured and computed current velocity in the vicinity of the SBW extremity, we address the complex wave transformation across the SBW and the impact on inshore rip currents. We further run the model during two representative real storms to address sediment transport patterns and further diagnose the morphological changes observed through video monitoring. After a brief description of the field site (Section 2), the data and method used to characterize the influence of SBW on nearshore hydrodynamics at Sète are given in Section 3. Results (Section 4) are discussed in Section 5 before conclusions are drawn.

2. Study Area

The Lido of Sète is a narrow coastal sandy barrier facing the Mediterranean Sea located in the northern part of the Gulf of Lions (Figure 1a). The studied coast (red box in Figure 1a) is a semidiurnal microtidal environment, with a moderate-energy modal wave climate and episodic severe storms. The annual mean significant wave height is 0.52 m while the 98% quantile reaches 2.2 m, defining the episodic storm signature with events typically characterized by wave periods around 8 s [32]. Waves associated with storms do not exceed 3.5% of occurrences and arrive mainly from ESE (77% of occurrences), almost normal to the coastline, while storms from the S are less frequent (16% of occurrences) [34].

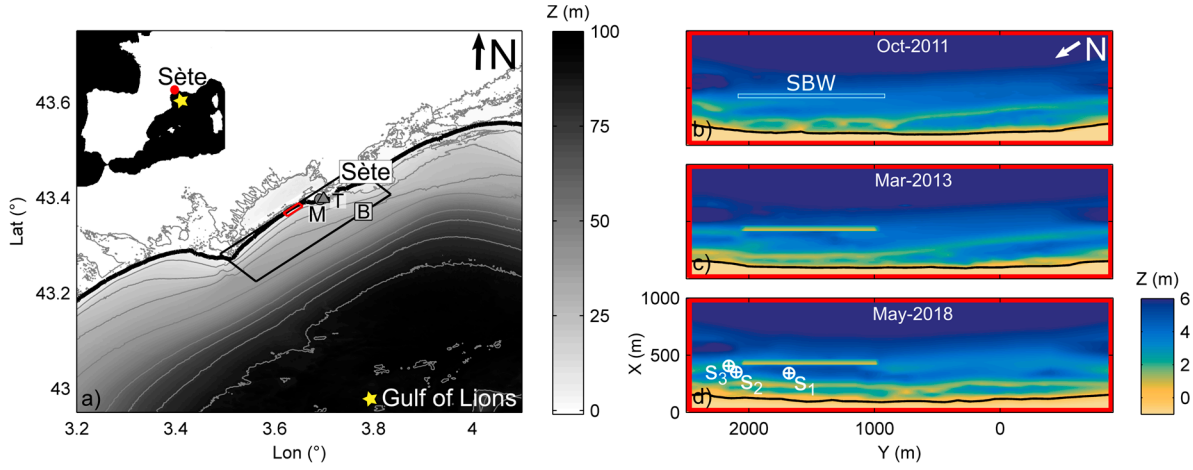

Figure 1. Large-scale (**a**) and nearshore-scale (**b**–**d**) bathymetries, which were further used for the computations. (**a**) Bathymetry of the Gulf of Lions (copyright Service Hydrographique et Océanographique de la Marine (SHOM)) with the directional wave buoy (B), meteorological station (M), and tidal gauge (T) locations indicated. (**b**–**d**) High-resolution bathymetry of the measurement site in local coordinates with the submerged breakwater (SBW) and instrument locations indicated.

The Lido of Sète has experienced chronic marine erosion during the last decades, with a 50 m beach retreat in less than 50 years [35]. This is particularly problematic as the beach system is of major interest from the perspective of socio-economic activity with an attendance of up to 1 million beachgoers per year [36]. A large beach management program was developed at the Lido to fight against chronic

erosion [37] involving the installation of an SBW 800 m in length in early 2013 (extended to 1 km shortly after) on the subdued outer bar located 350 m from the shore (Figure 1b). The breakwater consists of two rows of sand containers 50 m in length and 6 m in width, extending 1 km and 12 m in the alongshore and cross-shore directions, respectively. It is 3 m high, with its crest in approximately 2 m water depth [32].

The impact of the SBW has been previously investigated using a series of topo-bathymetric data [38] and video monitoring [32]. Observations indicated that the structure had a profound impact on nearshore system morphological behavior. In the protected sector just shoreward of the reef, the initially crescentic and slightly oblique sandbar located close to the shore initiated a clockwise rotation and became progressively linear predominantly under high wave energy events (Figure 1b–d). One kilometer away, southwestward along the adjacent coast, the inner bar pursued its natural net offshore migration (NOM) cycle. Such contrasted cross-shore behaviors between the two sectors led to the split of the entire inner bar a few hundred meters away from the SBW extremity. The typical formation of a salient was not observed. Instead, shoreline coupled to the new alongshore uniform sandbar geometry, which resulted in a slight seaward migration of the shoreline in the lee of the SBW.

3. Data & Methods

3.1. Field Measurements (April–May 2018 Field Campaign)

A field experiment was conducted at the Lido of Sète during almost one month from 27 April to 25 May 2018 to address the hydrodynamics in the vicinity of the SBW. The experiment consisted of two *Nortek* Aquadop profilers (S1 and S3 Figure 1d, sampled at 2 MHz) and one *RDI* (RD Instrument) acoustic Doppler profiler (S2 Figure 1d, 1200 KHz) moored in 5, 3, and 4.5 m depths, respectively. All instruments were set up from a boat at a location determined by preliminary numerical modeling experiments indicating potential locations to capture relevant wave-driven circulation patterns. While the southwest extremity of the SBW was not accessible during the measurement period because of coastal work on the SBW in this sector, the three acoustic Doppler profilers were deployed around the northeast side (Figure 1d). For all instruments, velocity measurement accuracy was about ±0.1 m/s. Velocity data were averaged over 15 min in the entire water column and decomposed into 30 cm vertical cells.

A few days after instrument deployment (gray line in Figure 2), a bathymetric survey was performed consisting of approximately 100 m spaced echo sounding transects. Vertical and horizontal accuracy were about ±0.05 m and 1 m, respectively, for each survey point. The survey area extended from the very nearshore area (almost at the shoreline) to 10 m water depth offshore and extended 3.5 km alongshore (Figure 1d).

A directional wave buoy moored approximatively 10 km off the study site provided hourly incident swell conditions (B in Figure 1a). Water levels were measured every 30 min in the harbor of Sète (T in Figure 1a) and a meteorological station recorded hourly mean wind conditions a few kilometers away from the study site (M in Figure 1a).

3.2. Model and Simulation Setup

3.2.1. Numerical Morphodynamic Model

Here we used the morphodynamic model 2DBeach described in [39] that described nearshore hydrodynamics, coupling a spectral wave model with a short-wave-averaged and depth-integrated flow model. Hydrodynamics in turn drove a model addressing sediment transport and bottom changes that looped back in the hydrodynamics. 2Dbeach is briefly described below.

- Wave module

The wave field was computed from the spectral wave model SWAN (41.10 version) [40], which solved the spectral wave-action balance. Radiation stress components, which drove

set-up/set-down and nearshore circulations, were computed on the same computational grid as that of the nearshore circulation, which was nested in a larger and coarser wave grid (Section 3.2.2).

- Circulation module

The circulation module was the same as in [39]. It was based on the depth- and phase-averaged nonlinear shallow water equations using an implicit method to obtain quasi-steady mean water depth and water volume flux [41]. The shallow water equations comprised the water mass conservation and momentum conservation equations, which, using the Einstein summation convention, read:

$$\frac{\partial Q_i}{\partial t} + \frac{\partial}{\partial x_j}\left(\frac{Q_i Q_j}{h}\right) + gh\frac{\partial \eta}{\partial x_j} + \frac{1}{\rho}\frac{\partial S_{ij}}{\partial x_j} - \frac{1}{\rho}\frac{\partial T_{ij}}{\partial x_j} + \frac{\Gamma_i^b}{\rho} = 0, \tag{1}$$

$$\frac{\partial \eta}{\partial t} + \frac{\partial Q_j}{\partial x_j} = 0, \tag{2}$$

where h is the mean water depth and $Q_i = hU_i$ is the water volume fluxes with subscript i referring to the two horizontal coordinates (x and y). U_i is the depth-averaged velocity according to Mei et al. [42]. Bed return flow can also be computed according to Phillips [43]. η is the mean surface elevation, g is the gravitational acceleration, ρ the water density, and S_{ij} the radiation stress tensor [43]. The bed shear stress tensor Γ_i^b is described according to Phillips [43],

$$\Gamma_i^b = \rho C_f U_{rms} U_i, \tag{3}$$

where U_{rms} is the root-mean-square wave orbital velocity at the bottom and C_f is a bottom friction coefficient. T_{ij} is the lateral mixing term which describes the horizontal momentum exchange due to the combined action of turbulence and mean current, using the formulation proposed by Battjes [44]:

$$T_{ij} = \rho h \nu \left(\frac{\partial U_i}{\partial x_j} + \frac{\partial U_j}{\partial x_i}\right), \tag{4}$$

where ν defines the eddy viscosity,

$$\nu = Mh\left(\frac{D}{\rho}\right)^{\frac{1}{3}} + \nu_0, \tag{5}$$

where D is the rate of energy loss through depth-induced wave breaking; M is a dimensionless coefficient and ν_0 is a constant eddy viscosity.

- Sediment transport module

The sediment transport module computed the total sediment transport Q_{tot} with an energetics-type sediment transport equation, based on [45] and [46], consisting of three modes [47] reading:

$$Q_{tot} = Q_w + Q_c - Q_d, \tag{6}$$

with transports related to wave velocity skewness Q_w, wave-induced mean current Q_c, and gravitational downslope effects Q_d. Each mode of transport contained both bed load and suspended load [47]. The bed level was updated through the sediment mass conservation equation that looped back into the wave model.

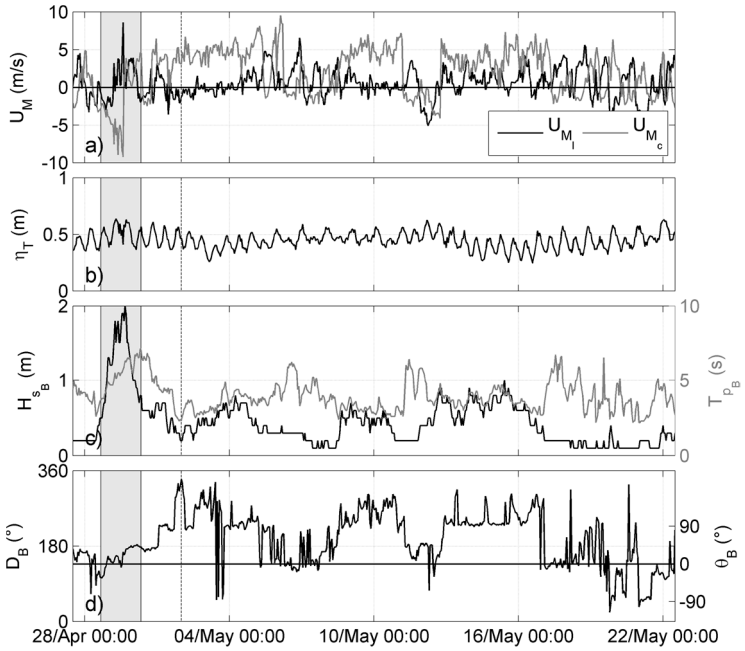

Figure 2. Time series of wind velocity (**a**); water levels (**b**); offshore significant wave height H_{s_B} and peak period T_{p_B} (**c**); and wave direction D_B and angle of wave incidence with respect to shore-normal θ_B (**d**) during the field experiment. Wind velocity and direction are decomposed into longshore (U_{M_L}, positive northeastward) and cross-shore wind velocity components (U_{M_C}, positive onshore). Water levels (η_T) are given with respect to lowest astronomical tide reference. The vertical gray line indicates the date of a bathymetric survey.

3.2.2. Model Setup

The implementation of the modeling system at Sète involved two nested Cartesian grids: one large coarse grid (30100 m × 8800 m; 100 m × 100 m meshes; black box in Figure 1a) for the offshore wave model (1) and a nested, finer grid (3400 m × 1000 m; 10 m × 10 m meshes; red box in Figure 1a) for the nearshore circulation (2) and sediment transport model (3).

(1) The wave field was computed from the wave buoy (B in Figure 1a) to a 10 m depth using an hourly spatially constant tidal range (T in Figure 1a) and spatially averaged wind forcing (M in Figure 1a). The bathymetry of the continental shelf was provided by the SHOM (Service Hydrographique et Océanographique de la Marine). Wind effects were activated through a linear wind wave growth [48] and a linear dissipation by whitecapping [49]. Energy lost from bottom friction was computed using Madsen et al. [50] with a default constant bottom roughness length scale of $Kn = 0.05$.

(2) Nearshore waves and currents were computed on the fine grid, using lateral periodic conditions for the circulation module. Different representative nearshore bathymetries were used, all derived from bathymetric surveys, and depicting different steps of the morphological changes observed following SBW implementation (Section 3.3). To complete the survey in shallow water, the shoreline was extracted from video images (Section 3.3) using a shoreline detection method based on a boundary extraction procedure from the automatic segmented coastal area [51]. Given the abrupt water depth changes across the SBW, owing to the sandbag shape, the structure was implemented schematically according to grid resolution. Energy loss due to depth-induced breaking was computed with the dissipation model of [52] with a constant breaker parameter $\gamma = 0.73$ [53]. To avoid non-physical wave refraction at the SBW extremities, limiters ($l = 0.25$) were used for spectral wave propagation [54]. Hydrodynamic free parameters C_f, ν_0, and M, were tuned to give the best agreement of the simulations with the field measurements (Section 4.2). To objectively assess model skill, linear squared-correlation (R^2), root mean square error (RMSE), and Brier skill score (BSS [55]) between the observed and simulated current velocities were computed (Table 1).

Table 1. Performance of the hydrodynamic model during the storm.

Station	BSS	RMSE	R^2	std (V_{obs})
$V_{l_{s1}}$	0.52	0.06	0.26	0.07
$V_{l_{s2}}$	0.83	0.08	0.63	0.13
$V_{l_{s3}}$	0.45	0.08	0.33	0.11
$V_{c_{s1}}$	0.13	0.05	0	0.04
$V_{c_{s2}}$	0.33	0.07	0	0.07
$V_{c_{s3}}$	0.77	0.10	0.42	0.14

(3) The total sediment transport was computed with a spatially constant *d50* of 250 µm in agreement with the beach grain size at the Lido of Sète. Coefficients C_w, C_c, and C_d that scaled the contribution of each corresponding transport (Q_w, Q_c, and Q_d, respectively) were adjusted following a sensitivity analysis. From default coefficients (C_w:C_c:C_d = 0.08:0.08:0.24), we adopted C_w:C_c:C_d = 0.005:0.08:0.24.

3.3. Video Data and Historical Storm Events Scenario

An Argus video monitoring system [56] consisting of eight cameras had been collecting images of the beach of Sète since mid-April 2011 [32,57]. Ten minute averaged images were merged and transformed into real world coordinate plan view images [58] extending 650 m in the cross-shore and 3550 m in the alongshore directions (Figure 3a). Sandbar crest positions were extracted before and after every energetic event through the sampling of pixel luminosity intensity [26]. Figure 3 illustrates the morphological response of the inner bar to the SBW implementation with Figure 3a–e showing the time exposure plan view at different dates. In order to provide a measure of the inner bar's morphological change from a given initial situation, the inner bar morphological change index (IM_{XBar}, Figure 3f) was computed as:

$$IM_{XBar} = \sqrt{\sum_{yargus=1}^{N} \left(X_{t_{yargus}} - X_{ref_{yargus}}\right)^2 / N}, \quad (7)$$

with X_{t_yargus} the cross-shore sandbar position along the time and $X_{ref_{yargus}}$ a reference, here the initial bar extracted.

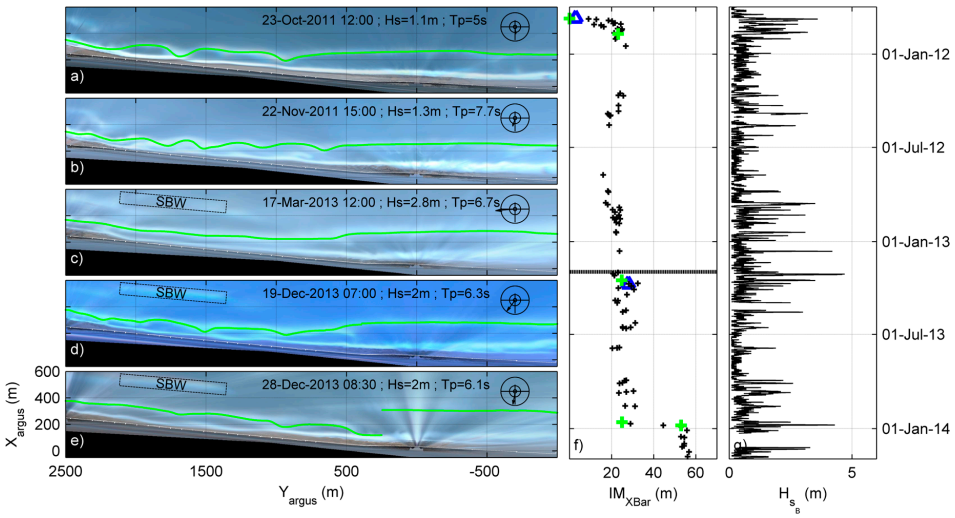

Figure 3. (**a**–**e**) Plan view time-exposure images showing inner bar morphology (green curve) and SBW position. (**f**) Temporal evolution of the inner bar change index (IM_{XBar}). Green crosses indicate the date and value obtained from the illustrated time exposure panels (**a**–**e**), while blue triangles correspond to the date and value computed from bathymetric surveys. Black dashed line corresponds to the date of SBW implementation. (**g**) Temporal evolution of significant wave height (H_{s_B}) measured at the offshore wave buoy location.

Within the entire time series shown in Figure 3, the October 2011 and December 2013 storm events stood out in terms of inner bar morphological changes (Figure 3f). The October 2011 event was characterized by energetic waves from ESE ($\theta_B \sim -14°$) with significant wave height and peak wave period reaching 3.7 m and 8.1 s, respectively. This event, when the SBW was not implemented yet, drove the development of inner bar rip channels and a slight onshore sandbar migration (Figure 3a,b). The December 2013 event was characterized by energetic waves from the S ($\theta_B \sim 32°$) with significant wave height and peak period reaching 4.3 m and 8 s, respectively. This event drove the inner bar splitting next to the SBW and inner bar straightening in its lee (Figure 3d,e). These two events were modeled (Section 4.4) with and without the SBW to address the impact of its implementation on nearshore hydrodynamics and morphological response using representative nearshore bathymetries surveyed before each storm (blue triangles in Figure 3f).

3.4. Residual and Vorticity Forcing

The influence of the SBW on wave-driven circulation was addressed with two approaches:

(1) The first approach was based on the combination of radiation stress gradients ($\vec{F}_w = -\frac{1}{\rho}\frac{\partial S_{ij}}{\partial x_j}$) and pressure gradients ($\vec{F}_p = -gh\frac{\partial \eta}{\partial x_i}$). Previous works showed that the major driving mechanism for nearshore circulation was the vectoral sum of the two components (F_{ri}), as it indicated how much net forcing was available to drive nearshore currents [39,41]:

$$F_{ri} = -gh\frac{\partial \eta}{\partial x_i} - \frac{1}{\rho}\frac{\partial S_{ij}}{\partial x_j}. \quad (8)$$

(2) The second approach was based on the differential broken wave energy dissipation derived from the depth-integrated and time-averaged momentum equations. Previous studies showed that the strength and rotational nature of nearshore circulations were essentially governed by the wave-induced vorticity forcing terms F_D [18,39]:

$$F_D = \left(\vec{\nabla} \wedge \left[\frac{D^r}{\sigma_r \rho \bar{h}}\vec{k}\right]\right)\cdot\vec{e_z}, \quad (9)$$

where D^r is the roller energy dissipation, σ_r the relative frequency, and k the wave number. The vorticity forcing terms, therefore, provide better insight on the origin of nearshore circulation without having to consider pressure gradients (no need to run a circulation model).

4. Results

4.1. Wave-Driven Circulation Measurements

During the field campaign, the bathymetry exhibited a reasonably alongshore uniform double bar system (Figure 1d) that barely evolved throughout the measurement period. The well-developed inner bar was located 150 m from the shore with its crest 1.5 m in depth. The subdued outer bar was aligned with the submerged breakwater approximatively 300 m from the shore with its crest 3.5 m in depth. During the experiment, one energetic event with H_{s_B} reaching 2 m was captured around 29 April (Figure 2c). During that period (shaded area in Figure 2), the beach of Sète was exposed to relatively energetic and obliquely incident waves coming from the south ($\theta_B \sim 26°$) with short peak wave periods ($T_{p_B} \sim 6$ s). The rest of the field campaign was characterized by strong offshore winds generating seaward propagating waves and low-incident wave energy. Therefore, hereafter only the hydrodynamics during the energetic event were described.

A detailed inspection of pitch deviation of S3 indicated that at approximately 10:00 on 29 April the sensor strongly deviated vertically. Therefore, subsequent S3 data were removed from the analysis. Figure 4 shows that, for all instruments, a strong change in longshore velocities occurred on 29 April. While prior to 29 April 00:00 weak negative longshore currents were measured, velocities dramatically

increased as a result of the increased wave height (Figure 4b), and concurrent changes in wave direction (Figure 4c). During the rest of the experiment, the longshore current remained positive with intensity ranging from 0 to 0.4 m/s depending on instrument location. It was important to note the reasonable vertical uniformity of flow velocities when the longshore current became significant (V_l > 0.3 m/s), giving confidence in the application of a 2DH model to simulate longshore currents. Substantial positive cross-shore currents were measured, particularly at S3 with velocity reaching 0.4 m/s close to the peak of the event, with substantial variability within the water column.

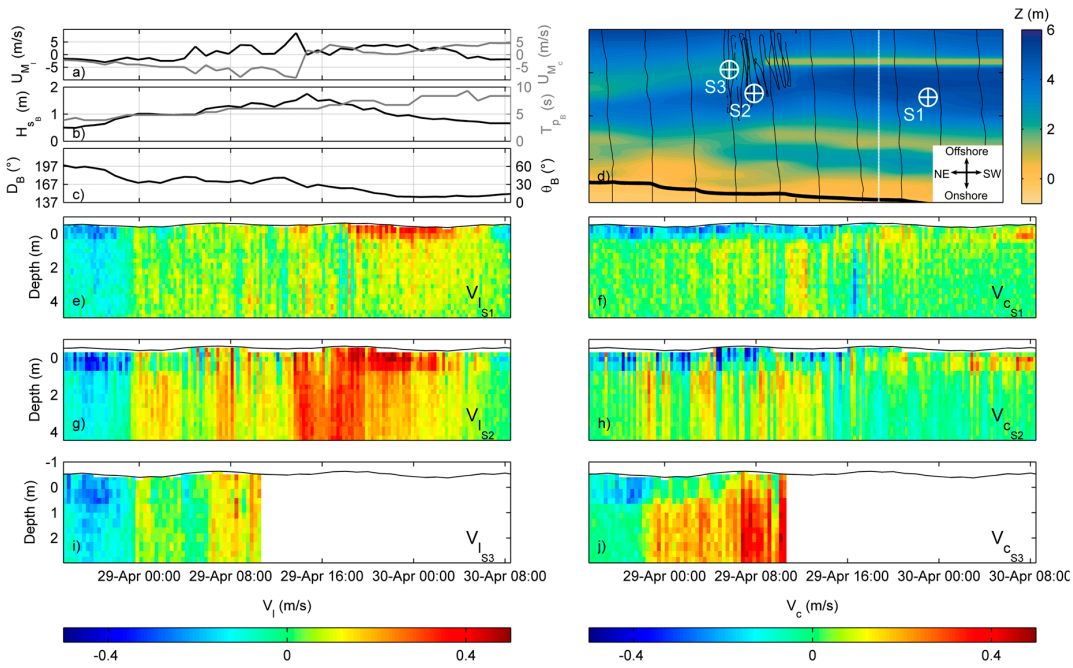

Figure 4. Times series of wind velocity (**a**); offshore significant wave height H_{s_B} and peak period T_{p_B} (**b**); wave direction D_B and angle of wave incidence with respect to shore-normal θ_B (**c**) along the energetic event; (**d**) bathymetry of the instrumented barred morphology around the SBW (black lines illustrate the bathymetric survey); and (**e**–**j**) vertical profile of longshore (V_l) and cross-shore (V_c) current velocities ($V_{l_{S1}}$ to $V_{c_{S3}}$).

4.2. Model Calibration/Validation

To test the ability of the model to accurately simulate wave-induced currents around the SBW, the measured flow was depth-integrated and averaged on a period larger than typical very low-frequency pulsations (moving average of 30 min). Model calibration was realized by tuning the bottom friction coefficient C_f, which controlled flow intensity, and the mixing terms ν_0 and M, which affected the shape and size of the horizontal circulation. The best agreement with field data was found for C_f = 0.012, ν_0 = 10 m^2·s^{-1}, and M = 5 and was within the range of earlier studies [39,41].

Figure 5 shows the time evolution of the computed/measured flow intensity. During low-energy conditions (H_{s_B} < 1 m), the model indicated that waves did not break across the SBW (Figure 5b) with near-zero flow velocities (Figure 5c–e). When wave energy increased, waves broke across the reef resulting in systematically low-energy waves in the lee (Figure 5b). Despite an increase in wave energy offshore, measured and modeled flow velocities remained weak (<0.1 m/s) at S1. At S2, velocities were much more variable in time. The longshore current reached 0.4 m/s around the peak of the event (Figure 5d) and varied slightly in intensity depending on the offshore wave energy and direction. Variations in magnitude were well reproduced by the model (BSS = 0.83, RMSE = 0.08 and R^2 = 0.63 in Table 1). In the cross-shore direction, flow velocities were also simulated with fair accuracy. Cross-shore, offshore-directed flows were stronger at S3, with a maximum close to 0.4 m/s. While the

model underestimated cross-shore velocities at this location, the weak longshore flow component was fairly simulated.

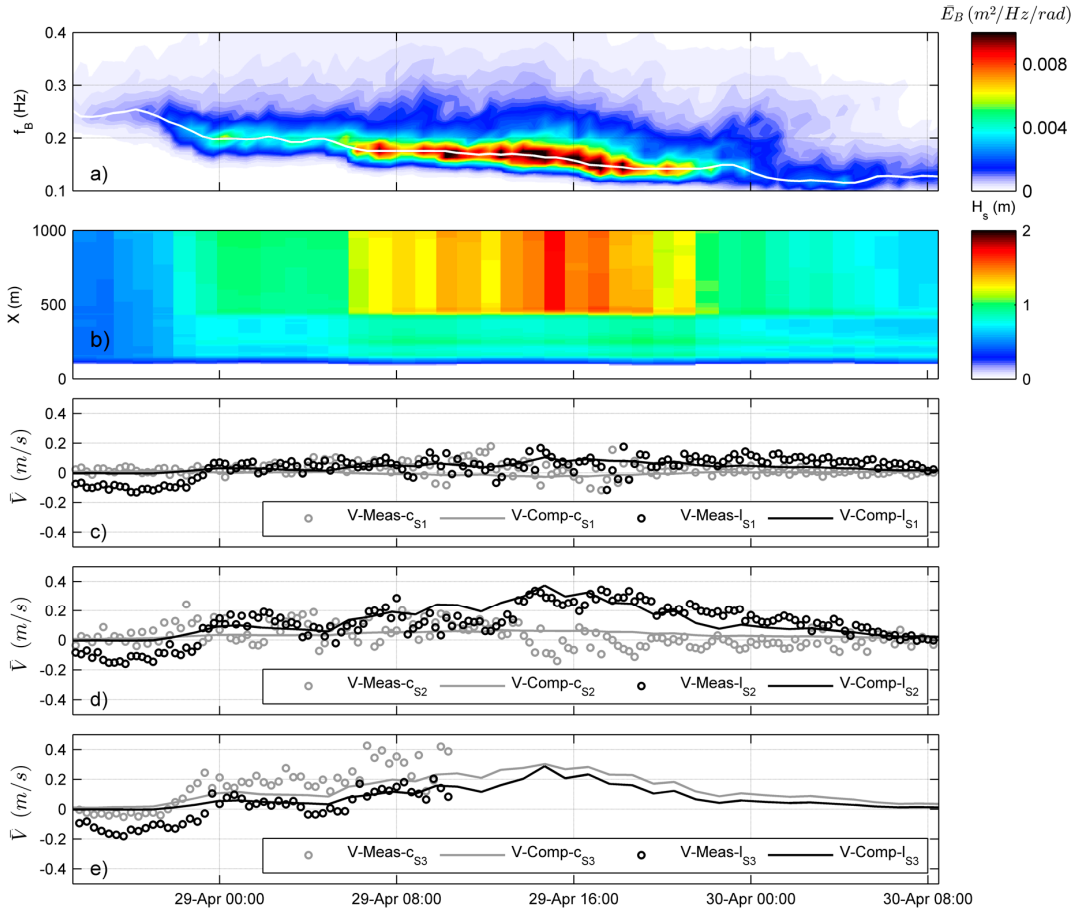

Figure 5. Comparison of measured (dots) and computed (line) flow quantities during storm. (**a**) Offshore wave energy measured by the buoy and (**b**) computed significant wave height through a cross-shore transect located in the SBW area (white transect Figure 4d). Panels (**c**–**e**) show in black (grey) the depth-averaged alongshore (cross-shore) velocity component (wave return flow activated in equations).

Results indicated that the model was more skillful in simulating longshore current when the wave heights increased. In contrast, non-surprisingly, the cross-shore currents, which were vertically non-uniform, were poorly reproduced. Observations and simulations clearly indicated the generation of a circulation at the extremity of the SBW when waves broke across the SBW. This is addressed in more detail in Section 4.3.

4.3. Driving Mechanisms of Rip-Cell Circulation at the Extremities of the Submerged Breakwater (SBW)

Figure 6 shows the hydrodynamic patterns during the field experiment at the peak of the event for offshore waves with $H_{s_B} = 2$ m, $T_{p_B} = 6.3$ s, and $\theta_B = 26°$. Intense depth-induced breaking across the SBW resulted in an important decrease in the significant wave height (Figure 6b) and large wave set-up (Figure 6c) in its lee. In the regions adjacent to the SBW, the onset of breaking (primarily across the inner bar), and resulting wave set-up, was observed much closer to the shore, resulting in highly variable pressure gradients $\vec{F_p}$ (Figure 6c). The imbalance between radiation stress gradients $\vec{F_w}$ and pressure gradients $\vec{F_p}$, namely residual forcing $\vec{F_r}$ (Section 3.4), indicated the net forcing available to drive nearshore currents. Clearly, this imbalance was maximized at the edges of the SBW (Figure 6d), where the vorticity forcing term F_D (Section 3.4) owing to alongshore variation in breaking wave energy was also maximized (Figure 6d). This meant that the dominant source of vorticity within the entire

nearshore domain was located at the edges of the SBW. More subtle sources were away from the SBW (Figure 6d) as a result of alongshore variability in depth-induced breaking enforced by the alongshore variability in depth of the inner bar. This resulted in the mean circulation field shown in Figure 6e, with dominant circulation at the edges of the SBW.

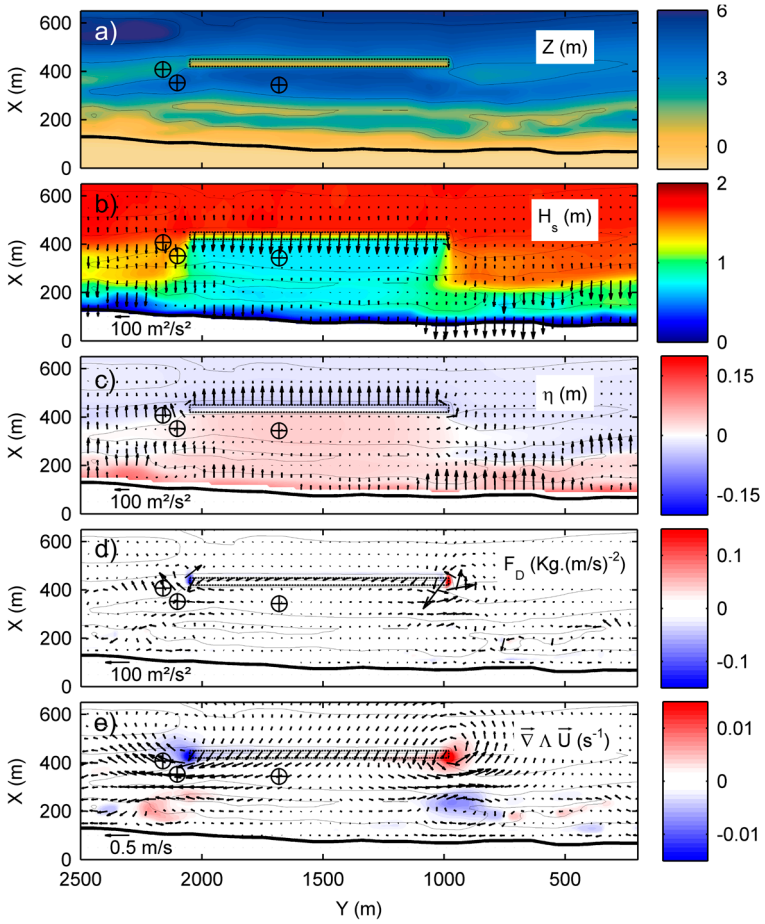

Figure 6. Hydrodynamics pattern at the peak of the event for offshore waves with $H_{s_B} = 2$ m, $T_{p_B} = 6.3$ s, and $\theta_B = 26°$. (**a**) Nearshore bathymetry; (**b**) significant wave height field colored and resulting gradients in radiation stress $\vec{F_w}$ (arrows); (**c**) pressure gradients $\vec{F_p}$ (arrows) superimposed on the mean surface elevation field (η) colored; (**d**) residual forcing $\vec{F_r}$ (arrows) superimposed on the vorticity forcing term field related to differential broken wave energy dissipation F_D; and (**e**) resulting wave-driven circulations $\vec{U}$ (arrows) and vorticity ($\vec{\nabla} \wedge \vec{U}$).

4.4. Hydrodynamics During Representative Severe Storms

4.4.1. The October 2011 Event

During the storm, the initial crescentic patterns slightly developed and migrated westward by a few hundred meters alongshore (Figure 3a,b). Figure 7 shows the wave-driven circulation and vorticity over the inner bar during the growth of the October 2011 storm event with H_s, T_p, and θ reaching 2 m, 7.5 s, and 8° at the nested offshore grid boundary. Simulations were performed without (left-hand panels) and with (right-hand panels) the SBW based on a bathymetry surveyed a few days before the storm to address the potential impact of the SBW under such event.

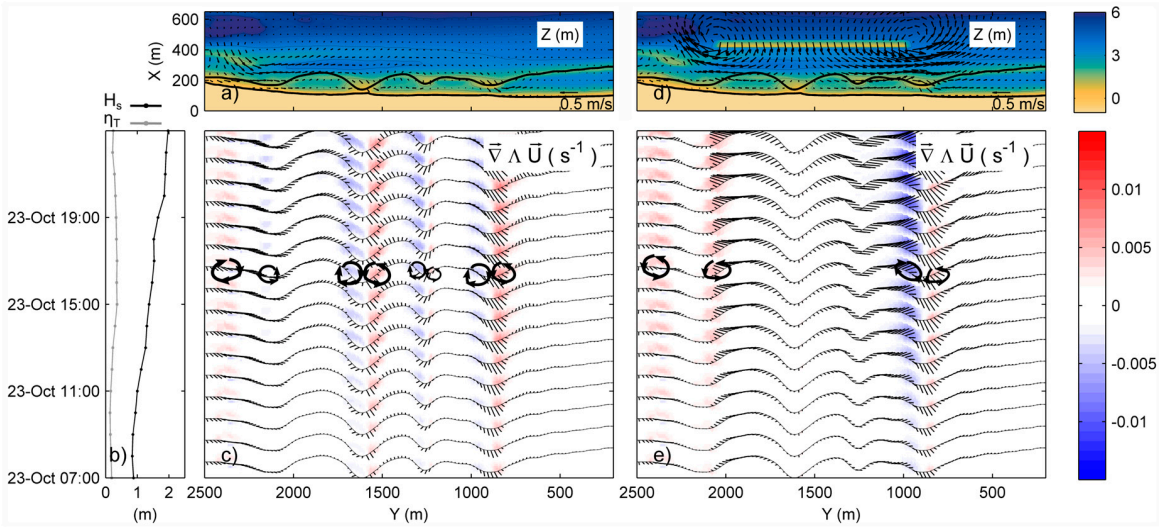

Figure 7. Wave-driven circulation during October 2011 storm without (left) and with SBW (right). (**a**,**d**) Bathymetry with the inner-bar crest location (black line) superimposed and resulting wave driven circulations $\vec{U}$ (arrows) at the storm peak. (**b**) Time series of offshore wave height (H_s) and water level (η_T) at the nested grid boundary. (**c**,**e**) Time series of vorticity $\vec{\nabla} \wedge \vec{U}$ across the inner bar superimposed on the current field velocity (arrows). Thick looped arrows indicate the dominant rotational characteristic of the flow.

Without the SBW, classic rip-flow patterns were observed across the rip-channeled inner bar owing to near-normal wave incidence. This resulted in positive and negative vorticity alternating alongshore (Figure 7c), close to the shore, with onshore and offshore flow across the shoals and deeper channels, respectively. Such a well-developed rip-cell system typically resulted in a positive feedback mechanism between flow (waves and current), sediment transport, and the evolving bathymetry that resulted in the further growth of the rip channels, as observed in (Figure 3a,b). In contrast, in line with the simulation shown in (Section 4.3), implementing the SBW resulted in a larger number of offshore and more intense rip-cell circulations observed at the edges of the SBW (Figure 7d) where the vorticity field was maximized (Figure 7e). In the lee of the SBW, depth-induced breaking across the inner bar was negligible, as waves mostly dissipated further offshore across the SBW. These low-energy waves could not drive rip-cell circulation over the reasonably well-developed inner-bar rip channels. Instead, the circulation over the inner bar was dominated by a longshore current, which, very likely, drove the progressive straightening of the inner-bar rip channels observed after SBW implementation.

4.4.2. The December 2013 Event

The December 2013 storm event led to an important net offshore sandbar migration at a few hundred meters from the SBW, while the morphology remained stable in its lee, resulting in sandbar splitting (Figure 3d,e). Figure 8 shows the wave-driven circulation and the computed sediment transport at the peak of the December 2013 storm event with H_s = 3 m, T_p = 9.3 s, and θ = 21° at the nested offshore grid boundary. For this simulation, differences in cross-shore sandbar migration needed to be addressed carefully. Because cross-shore sandbar migration is primarily triggered by the imbalance between onshore sediment transport, driven by wave nonlinearities, and offshore sediment transport, driven by the undertow, sediment transport and morphological changes were switched on.

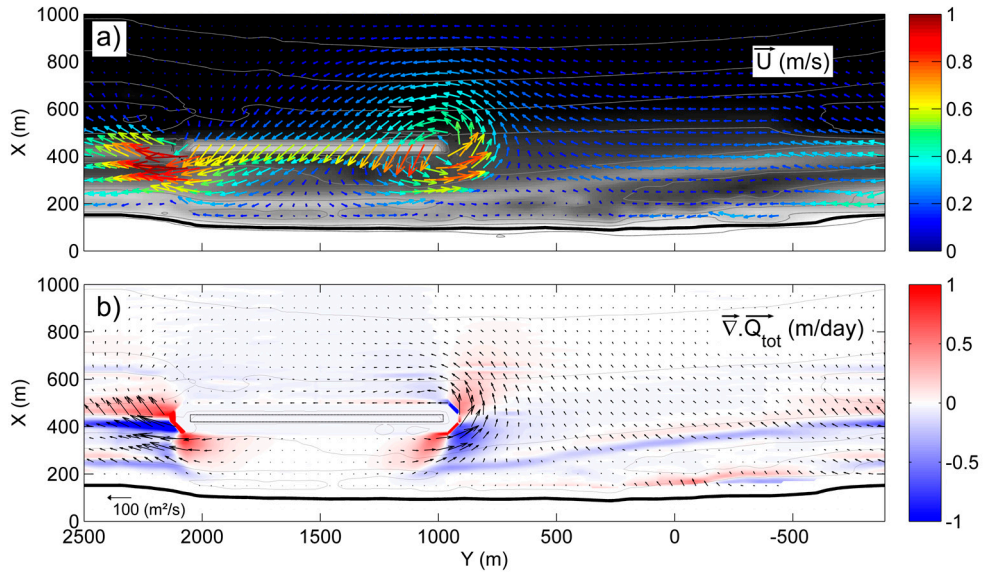

Figure 8. Hydrodynamics and sediment transport at the peak of the December 2013 storm event for offshore waves with $H_s = 3$ m, $T_p = 9.3$ s, and $\theta = 21°$ at the nested grid boundary. (**a**) Resulting wave-driven circulations $\vec{U}$ (arrows) and (**b**) erosion/accretion patterns ($\vec{\nabla}.\vec{Q}_{tot}$) driven by the total sediment transport with the arrows indicating the sediment fluxes.

Although intense rip-cell circulations at the edges of the SBW were still observed (Figure 8a), sediment transport patterns and resulting morphological changes shed light onto the underlying driving mechanism of sandbar splitting (Figure 8b). In the lee of the SBW, low-energy waves resulted in almost no net sediment transport. In contrast, as a result of intense depth-induced breaking across the bar away from the SBW (e.g., at Y = −500 m in Figure 8b), offshore transport driven by the undertow dominated compared to onshore transport driven by wave nonlinearities. This resulted in sediment transport gradients forming erosion and accretion patterns at the shoreward and seaward part of the sandbar, respectively, which was the signature of offshore migration. Therefore, the dramatic change in cross-shore sediment transport patterns was induced in the lee of the SBW, inhibiting offshore migration, while the sandbar away from the SBW continued its natural NOM behavior, which was primarily triggered by storm events.

5. Discussion and Conclusions

The results presented in Section 4 showed that the SBW deployed at the beach of Sète induced large changes in hydrodynamics and sediment transport patterns in the nearshore area. Our results show that implementing such a shallow alongshore uniform SBW, with abrupt alongshore depth variabilities at both extremities, dramatically changes wave-driven patterns and resulting sediment transport pathways. Clearly, two counter-rotating rip-cell circulations dominate the nearshore hydrodynamics, pending waves are breaking across the reef. These circulations are essentially enforced by a strong alongshore differential broken wave energy dissipation. This contrasted with other, smoother, SBWs where the control of nearshore hydrodynamics was more subtle [59].

Despite it being based on a depth-averaged approach, the model skillfully simulates the circulation at the edges of the SBW, allowing to subsequently investigate the underlying processes driving observed sandbar straightening in the lee of the SBW and sandbar splitting nearby. Results suggest that depth-induced breaking wave energy dissipation across the SBW systematically results in low-energy waves in the lee of the SBW, even for moderate- to high-energy waves. Such systematically low-energy waves across the inner bar in the lee of the SBW cannot drive rip current circulation, and therefore cannot further develop or even sustain existing rip channels. To further test this hypothesis leading to inner bar straightening in the lee of the SBW, Figure 9 shows a morphodynamic simulation

starting from an alongshore uniform double-barred system based on Sète beach characteristics. One simulation was performed without the SBW (left-hand panel in Figure 9), and the other with the SBW implemented as a non-erodible structure (right-hand panels in Figure 9) for time-invariant, slightly oblique, incident moderate-energy waves. In line with existing nonlinear stability analysis of wave-dominated beaches [47,60–62], inner bar rip channels formed within a few days as positive feedback between the hydrodynamics (waves and current), sediment transport, and the evolving bathymetry. In contrast, with the SBW rip channels only developed apart from the SBW, in line with our hypothesis. Despite using a depth-averaged approach, using a nonlinear morphodynamic model appears relevant to predict the potential development of straightening of rip channels following the implementation of an SBW.

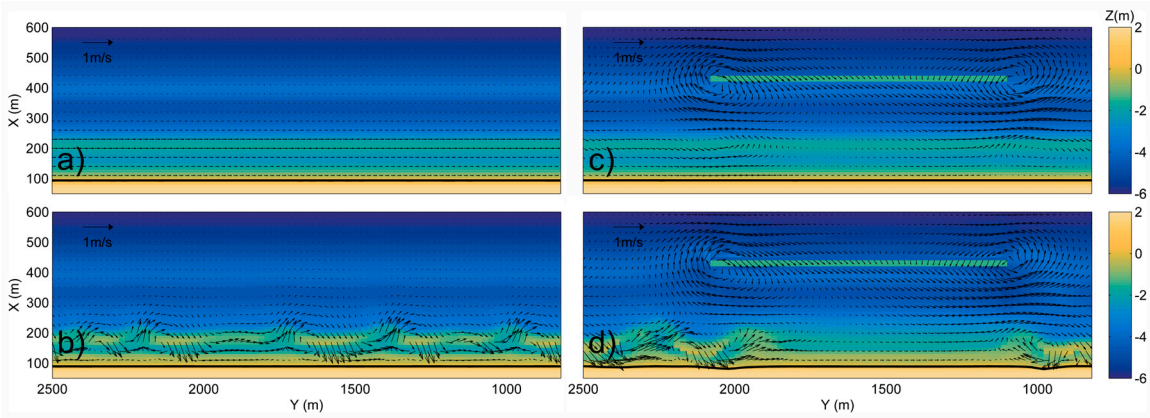

Figure 9. Bathymetry with superimposed wave-induced currents at (**a**,**c**) t = 0 h and (**b**,**d**) t = 50 h for waves with H_s = 1.5 m, T_p = 8 s, and θ = 15° starting from an alongshore uniform morphology for a beach without (left-hand panels) and with SBW (right-hand panels).

Following the implementation of the SBW at the beach of Sète, the bar continued its natural NOM cycle in the undisturbed sector while offshore migration was inhibited in the lee of the structure, resulting in bar splitting [32]. Our simulations show that, once again because of persistently low-energy breaking waves in the lee of the SBW, the imbalance between offshore sediment transport driven by the undertow and onshore by wave nonlinearities is inhibited. Therefore, in addition to the dramatic control on rip-cell circulation and resulting rip channel dynamics, the implementation of an SBW can also have a profound impact on cross-shore sediment and resulting cross-shore sandbar behavior. To our knowledge, such behavior had never been simulated so far. We therefore anticipate that the recent development of morphodynamic models, including a detailed description of cross-shore sand transport processes [47], can be used to predict the impact of SBWs on cross-shore sandbar behavior.

The influence of SBW on sandbar morphodynamics is critical to shoreline evolution. At Sète, the initial shoreline–sandbar coupling was still observed after the implementation of the SBW, and given that sandbar rhythmicity progressively disappeared, the shoreline realigned to the inner bar, resulting in 15 m beach widening within a year [32]. Overall, our results illustrate the importance of considering nearshore sandbars when designing coastal structures. The impact of the design of an artificial reef is complex and case-sensitive. The present work suggests that nonlinear morphodynamic models accurately describing the dynamics of surf zone sandbars are now mature to predict SBW impact on sandbar(s) and, in turn, on shoreline response.

Author Contributions: All co-authors have contributed substantially to the research concept, field campaign and to the execution of the numerical experiment. Y.B. provided his expertise in operational storm event forecasting. Y.B. and C.B. setup and performed the field experiments and analyzed field measurements. B.C. provided his expertise on numerical modeling. C.B. and B.C. designed the numerical modeling experiments and analyzed model results.

Funding: This research was funded by financial support from BRGM, DREAL-Occitanie, and Sète AggloPôle Méditerranée through a PhD grant. This research received also external funding from Agence National de la Recherche (ANR) grant ANR-17-CE01-0014 (SONO project).

Acknowledgments: C.B. and B.C. gratefully acknowledge B. Dubarbier for his technical support on 2DBeach numerical model. L. Desbiendras, J. Tesson, R. Belon, M. Giusti, Y. Colombet, P-A Picand, F. Longueville, A. Latapy, S. Hureau, and M. Guebba are greatly acknowledged for their help in processing video data. We thank the two anonymous reviewers for providing constructive feedback that helped improving our manuscript.

Conflicts of Interest: The authors declare no conflict of interest.

References

1. Charlier, R.H.; De Meyer, C.P. Coastal defense and beach renovation. *Ocean Shorel. Manag.* **1989**, *12*, 525–543. [CrossRef]
2. Nordstrom, K.F. Living with shore protection structures: A review. *Estuar. Coast. Shelf Sci.* **2014**, *150*, 11–23. [CrossRef]
3. Charlier, R.H.; Chaineux, M.C.P.; Morcos, S. Panorama of the History of Coastal Protection. *J. Coast. Res.* **2005**, *21*, 79–111. [CrossRef]
4. van Rijn, L.C. Coastal erosion and control. *Ocean Coast. Manag.* **2011**, *54*, 867–887. [CrossRef]
5. Black, K.P.; Andrews, C.J. Sandy Shoreline Response to Offshore Obstacles Part 1: Salient and Tombolo Geometry and Shape. *J. Coast. Res.* **2001**, 82–93. [CrossRef]
6. Evans, P.; Ranasinghe, R. Artificial Surfing Reefs: A New Paradigm in Coastal Protection? In Proceedings of the 15th Australasian Coastal and Ocean Engineering Conference, the 8th Australasian Port and Harbour Conference, Gold Coast, QLD, Australia, 25–28 September 2001; pp. 128–133.
7. Wamsley, T.; Hanson, H.; Kraus, N. *Wave Transmission at Detached Breakwaters for Shoreline Response Modeling*; ERDC/CHL CHETN-II45; U.S. Army Engineer Research and Development Center: Vicksburg, MS, USA, 2002.
8. Isebe, D.; Azerad, P.; Bouchette, F.; Ivorra, B.; Mohammadi, B. Shape optimization of geotextile tubes for sandy beach protection. *Int. J. Numer. Methods Eng.* **2008**, *74*, 1262–1277. [CrossRef]
9. Van der Meer, J.W.; Briganti, R.; Zanuttigh, B.; Wang, B. Wave transmission and reflection at low-crested structures: Design formulae, oblique wave attack and spectral change. *Coast. Eng.* **2005**, *52*, 915–929. [CrossRef]
10. Calabrese, M.; Vicinanza, D.; Buccino, M. 2D Wave setup behind submerged breakwaters. *Ocean Eng.* **2008**, *35*, 1015–1028. [CrossRef]
11. Sumer, B.M.; Fredsøe, J.; Lamberti, A.; Zanuttigh, B.; Dixen, M.; Gislason, K.; Di Penta, A.F. Local scour at roundhead and along the trunk of low crested structures. *Coast. Eng.* **2005**, *52*, 995–1025. [CrossRef]
12. Ranasinghe, R.; Turner, I.L. Shoreline response to submerged structures: A review. *Coast. Eng.* **2006**, *53*, 65–79. [CrossRef]
13. Tomasicchio, U. Submerged Breakwaters for the Defence of the Shoreline at Ostia Field Experiences, Comparison. In Proceedings of the 25th Conference on Coastal Engineering, Orlando, FL, USA, 2–6 September 1996; American Society of Civil Engineers: New York, NY, USA, 1996; pp. 2404–2417.
14. Lamberti, A.; Mancinelli, A. Italian Experience on Submerged Barriers as Beach Defence Structures. In Proceedings of the 25th Conference on Coastal Engineering, Orlando, FL, USA, 2–6 September 1996; American Society of Civil Engineers: New York, NY, USA, 1996; pp. 2352–2365.
15. Dean, R.; Chen, R.; Browder, A. Full scale monitoring study of a submerged breakwater, Palm Beach, Florida, USA. *Coast. Eng.* **1997**, *29*, 291–315. [CrossRef]
16. Johnson, H.K.; Karambas, T.V.; Avgeris, I.; Zanuttigh, B.; Gonzalez-Marco, D.; Caceres, I. Modelling of waves and currents around submerged breakwaters. *Coast. Eng.* **2005**, *52*, 949–969. [CrossRef]
17. Ranasinghe, R.; Turner, I.L.; Symonds, G. Shoreline response to multi-functional artificial surfing reefs: A numerical and physical modelling study. *Coast. Eng.* **2006**, *53*, 589–611. [CrossRef]
18. Bruneau, N.; Bonneton, P.; Castelle, B.; Pedreros, R. Modeling rip current circulations and vorticity in a high-energy mesotidal-macrotidal environment. *J. Geophys. Res. Ocean.* **2011**, *116*, C07026. [CrossRef]
19. Castelle, B.; Scott, T.; Brander, R.W.; McCarroll, R.J. Rip current types, circulation and hazard. *Earth-Sci. Rev.* **2016**, *163*, 1–21. [CrossRef]
20. Utizi, K.; Corbau, C.; Rodella, I.; Nannini, S.; Simeoni, U. A mixed solution for a highly protected coast (Punta Marina, Northern Adriatic Sea, Italy). *Mar. Geol.* **2016**, *381*, 114–127. [CrossRef]

21. Ranasinghe, R.; Larson, M.; Savioli, J. Shoreline response to a single shore-parallel submerged breakwater. *Coast. Eng.* **2010**, *57*, 1006–1017. [CrossRef]
22. Zanuttigh, B. Numerical modelling of the morphological response induced by low-crested structures in Lido di Dante, Italy. *Cost. Eng.* **2007**, *54*, 31–47. [CrossRef]
23. Thornton, E.B.; MacMahan, J.; Sallenger, A.H. Rip currents, mega-cusps, and eroding dunes. *Mar. Geol.* **2007**, *240*, 151–167. [CrossRef]
24. van de Lageweg, W.I.; Bryan, K.R.; Coco, G.; Ruessink, B.G. Observations of shoreline–sandbar coupling on an embayed beach. *Mar. Geol.* **2013**, *344*, 101–114. [CrossRef]
25. Castelle, B.; Marieu, V.; Bujan, S.; Splinter, K.D.; Robinet, A.; Sénéchal, N.; Ferreira, S. Impact of the winter 2013–2014 series of severe Western Europe storms on a double-barred sandy coast: Beach and dune erosion and megacusp embayments. *Geomorphology* **2015**, *238*, 135–148. [CrossRef]
26. Lippmann, T.C.; Holman, R.A. Quantification of sand bar morphology: A video technique based on wave dissipation. *J. Geophys. Res.* **1989**, *94*, 995. [CrossRef]
27. Alexander, P.S.; Holman, R.A. Quantification of nearshore morphology based on video imaging. *Mar. Geol.* **2004**, *208*, 101–111. [CrossRef]
28. Holman, R.A.; Symonds, G.; Thornton, E.B.; Ranasinghe, R. Rip spacing and persistence on an embayed beach. *J. Geophys. Res.* **2006**, *111*, C01006. [CrossRef]
29. Ruessink, B.G.; Pape, L.; Turner, I.L. Daily to interannual cross-shore sandbar migration: Observations from a multiple sandbar system. *Cont. Shelf Res.* **2009**, *29*, 1663–1677. [CrossRef]
30. Almar, R.; Castelle, B.; Ruessink, B.G.; Sénéchal, N.; Bonneton, P.; Marieu, V. Two- and three-dimensional double-sandbar system behaviour under intense wave forcing and a meso-macro tidal range. *Cont. Shelf Res.* **2010**, *30*, 781–792. [CrossRef]
31. Gallop, S.L.; Bryan, K.R.; Coco, G.; Stephens, S.A. Storm-driven changes in rip channel patterns on an embayed beach. *Geomorphology* **2011**, *127*, 179–188. [CrossRef]
32. Bouvier, C.; Balouin, Y.; Castelle, B. Video monitoring of sandbar-shoreline response to an offshore submerged structure at a microtidal beach. *Geomorphology* **2017**, *295*, 297–305. [CrossRef]
33. Balouin, Y.; Tesson, J.; Gervais, M. Cuspate shoreline relationship with nearshore bar dynamics during storm events—Field observations at Sete beach, France. *J. Coast. Res.* **2013**, *65* (Suppl. 1), 440–446. [CrossRef]
34. Gervais, M.; Balouin, Y.; Belon, R. Morphological response and coastal dynamics associated with major storm events along the Gulf of Lions Coastline, France. *Geomorphology* **2012**, *143*, 69–80. [CrossRef]
35. Certain, R.; Barusseau, J.P. Conceptual modelling of sand bars morphodynamics for a microtidal beach (Sète, France). *Bull. Soc. Geol. Fr.* **2005**, *176*, 343–354. [CrossRef]
36. Balouin, Y.; Rey-Valette, H.; Picand, P.A. Automatic assessment and analysis of beach attendance using video images at the Lido of Sète beach, France. *Ocean Coast. Manag.* **2014**, *102*, 114–122. [CrossRef]
37. BCEOM. *Etude générale pour la protection et l'aménagement durable du lido de Sète à Marseillan, Synthèse générale*; Artelia: Marseille, France, 2001.
38. Bouvier, C.; Balouin, Y.; Castelle, B. Nearshore bars and shoreline dynamics associated with the implementation of a submerged breakwater: Topo-bathymetric analysis and video assessment at the Lido of Sète beach. In Proceedings of the Coastal Dynamics, Helsingør Denmark, 12–16 June 2017; pp. 534–543.
39. Castelle, B.; Marieu, V.; Coco, G.; Bonneton, P.; Bruneau, N.; Ruessink, B.G. On the impact of an offshore bathymetric anomaly on surf zone rip channels. *J. Geophys. Res. Earth Surf.* **2012**, *117*, f1. [CrossRef]
40. Booij, N.; Ris, R.C.; Holthuijsen, L.H. A third-generation wave model for coastal regions: 1. Model description and validation. *J. Geophys. Res. Ocean.* **1999**, *104*, 7649–7666. [CrossRef]
41. Castelle, B.; Bonneton, P.; Sénéchal, N.; Dupuis, H.; Butel, R.; Michel, D. Dynamics of wave-induced currents over an alongshore non-uniform multiple-barred sandy beach on the Aquitanian Coast, France. *Cont. Shelf Res.* **2006**, *26*, 113–131. [CrossRef]
42. Mei, C.; Stiassnie, M.; Yue, D. *Theory and Applications of Ocean Surface Waves: Part 1: Linear Aspects Part 2: Nonlinear Aspects*; World Scientific: Singapore, 1989; Volume 23, p. 506.
43. Phillips, O.M. *The Dynamics of the Upper Ocean*, 2nd ed.; Cambridge University Press: Cambridge, UK, 1977.
44. Battjes, J. Modeling of turbulence in the surf zone. In Proceedings of the Symposium on Modeling Techniques, ASCE, San Francisco, CA, USA, 3–5 September 1975; pp. 1050–1061.

45. Hsu, T.-J.; Elgar, S.; Guza, R.T. Wave-induced sediment transport and onshore sandbar migration. *Coast. Eng.* **2006**, *53*, 817–824. [CrossRef]
46. Dubarbier, B.; Castelle, B.; Marieu, V.; Ruessink, G. Process-based modeling of cross-shore sandbar behavior. *Coast. Eng.* **2015**, *95*, 35–50. [CrossRef]
47. Dubarbier, B.; Castelle, B.; Ruessink, G.; Marieu, V. Mechanisms controlling the complete accretionary beach state sequence. *Geophys. Res. Lett.* **2017**, *44*, 5645–5654. [CrossRef]
48. Cavaleri, L.; Rizzoli, P.M. Wind wave prediction in shallow water: Theory and applications. *J. Geophys. Res.* **1981**, *86*, 10961. [CrossRef]
49. Komen, G.J.; Hasselmann, K.; Hasselmann, K.; Komen, G.J.; Hasselmann, K.; Hasselmann, K. On the Existence of a Fully Developed Wind-Sea Spectrum. *J. Phys. Oceanogr.* **1984**, *14*, 1271–1285. [CrossRef]
50. Madsen, O.S.; Poon, Y.-K.; Graber, H.C. Spectral Wave Attenuation by Bottom Friction: Theory. In Proceedings of the 21st Conference on Coastal Engineering, Costa del Sol-Malaga, Spain, 20–25 June 1988; American Society of Civil Engineers: New York, NY, USA, 1989; pp. 492–504.
51. Valentini, N.; Saponieri, A.; Damiani, L. A new video monitoring system in support of Coastal Zone Management at Apulia Region, Italy. *Ocean Coast. Manag.* **2017**, *142*, 122–135. [CrossRef]
52. Battjes, J.A.; Janssen, J.P.F.M. Energy Loss and Set-Up Due to Breaking of Random Waves. In Proceedings of the 16th Conference on Coastal Engineering, Hamburg, Germany, 27 August–3 September 1978; American Society of Civil Engineers: New York, NY, USA, 1978; pp. 569–587.
53. Battjes, J.A.; Stive, M.J.F. Calibration and verification of a dissipation model for random breaking waves. *J. Geophys. Res.* **1985**, *90*, 9159. [CrossRef]
54. Dietrich, J.C.; Zijlema, M.; Allier, P.-E.; Holthuijsen, L.H.; Booij, N.; Meixner, J.D.; Proft, J.K.; Dawson, C.N.; Bender, C.J.; Naimaster, A.; et al. Limiters for spectral propagation velocities in SWAN. *Ocean Model.* **2013**, *70*, 85–102. [CrossRef]
55. Davidson, M.A.; Splinter, K.D.; Turner, I.L. A simple equilibrium model for predicting shoreline change. *Coast. Eng.* **2013**, *73*, 191–202. [CrossRef]
56. Holman, R.A.; Stanley, J. The history and technical capabilities of Argus. *Coast. Eng.* **2007**, *54*, 477–491. [CrossRef]
57. Bouvier, C.; Balouin, Y.; Castelle, B.; Holman, R. Modelling camera viewing angle deviation to improve nearshore video monitoring. *Coast. Eng.* **2019**, *174*, 99–106. [CrossRef]
58. Holland, K.T.; Holman, R.A.; Lippmann, T.C.; Stanley, J.; Plant, N. Practical Use of Video Imagery in Nearshore Oceanographic Field Studies. *IEEE J. Ocean. Eng.* **1997**, *22*, 81–92. [CrossRef]
59. Duarte Nemes, D.; Fabián Criado-Sudau, F.; Nicolás Gallo, M.; Duarte Nemes, D.; Fabián Criado-Sudau, F.; Nicolás Gallo, M. Beach Morphodynamic Response to a Submerged Reef. *Water* **2019**, *11*, 340. [CrossRef]
60. Calvete, D.; Dodd, N.; Falqués, A.; van Leeuwen, S.M. Morphological development of rip channel systems: Normal and near-normal wave incidence. *J. Geophys. Res. Ocean.* **2005**, *110*, C10. [CrossRef]
61. Garnier, R.; Falqués, A.; Calvete, D.; Thiébot, J.; Ribas, F. A mechanism for sandbar straightening by oblique wave incidence. *Geophys. Res. Lett.* **2013**, *40*, 2726–2730. [CrossRef]
62. Castelle, B.; Ruessink, B.G. Modeling formation and subsequent nonlinear evolution of rip channels: Time-varying versus time-invariant wave forcing. *J. Geophys. Res. Earth Surf.* **2011**, *116*, f4. [CrossRef]